

Characterization of antisite defects and in-gap states in antiferromagnetic $MnSb_2Te_4$

Junming Zhang(张峻铭), Ming Xi(席明), Yuchong Zhang(张羽翀), Hang Li(李航), Jiali Zhao(赵佳丽), Hechang Lei(雷和畅), Zhongxu Wei(魏忠旭), and Tian Qian(钱天)

Citation: Chin. Phys. B, 2025, 34 (**7**): 076801. DOI: 10.1088/1674-1056/adcea3
http://cpb.iphy.ac.cn; http://iopscience.iop.org/cpb

What follows is a list of articles you may be interested in

Surface solitonic charge distribution on 2D materials investigated using Kelvin probe force microscopy technique based on qplus atomic force microscopy

Rui Song(宋睿), Feng Hao(郝峰), Jie Yang(杨杰), Lifeng Yin(殷立峰), and Jian Shen(沈健)
Chin. Phys. B, 2025, 34 (**5**): 056802. DOI: 10.1088/1674-1056/adbee8

Emergent 3×3 charge order on the Cs reconstruction of kagome superconductor CsV_3Sb_5

Xianghe Han(韩相和), Zhongyi Cao(曹钟一), Zihao Huang(黄子豪), Zhen Zhao(赵振), Haitao Yang(杨海涛), Hui Chen(陈辉), and Hong-Jun Gao(高鸿钧)
Chin. Phys. B, 2025, 34 (**1**): 016801. DOI: 10.1088/1674-1056/ad8fa1

Surface evolution of thermoelectric material KCu_4Se_3 explored by scanning tunneling microscopy

Yumin Xia(夏玉敏), Ni Ma(马妮), Desheng Cai(蔡德胜), Yuzhou Liu(刘宇舟), Yitong Gu(谷易通), Gan Yu(于淦), Siyu Huo(霍思宇), Wenhui Pang(庞文慧), Chong Xiao(肖翀), and Shengyong Qin(秦胜勇)
Chin. Phys. B, 2024, 33 (**8**): 086804. DOI: 10.1088/1674-1056/ad50c4

Superconducting state in $Ba_{(1-x)}Sr_xNi_2As_2$ near the quantum critical point

Chengfeng Yu(余承峰), Zongyuan Zhang(张宗源), Linxing Song(宋林兴), Yanwei Wu(吴彦玮), Xiaoqiu Yuan(袁小秋), Jie Hou(侯杰), Yubing Tu(涂玉兵), Xingyuan Hou(侯兴元), Shiliang Li(李世亮), and Lei Shan(单磊)
Chin. Phys. B, 2024, 33 (**6**): 066802. DOI: 10.1088/1674-1056/ad334a

Microscopic growth mechanism and edge states of monolayer 1T'-$MoTe_2$

Haipeng Zhao(赵海鹏), Yin Liu(刘隐), Shengguo Yang(杨胜国), Chenfang Lin(林陈昉), Mingxing Chen(陈明星), Kai Braun, Xinyi Luo(罗心仪), Siyu Li(李思宇), Anlian Pan(潘安练), and Xiao Wang(王笑)
Chin. Phys. B, 2024, 33 (**4**): 046801. DOI: 10.1088/1674-1056/ad16d5

RAPID COMMUNICATION

Characterization of antisite defects and in-gap states in antiferromagnetic $MnSb_2Te_4$

Junming Zhang(张峻铭)[1,2], Ming Xi(席明)[3,4], Yuchong Zhang(张羽翀)[1,2], Hang Li(李航)[1], Jiali Zhao(赵佳丽)[1], Hechang Lei(雷和畅)[3,4,†], Zhongxu Wei(魏忠旭)[1,‡], and Tian Qian(钱天)[1,§]

[1] *Beijing National Laboratory for Condensed Matter Physics, Institute of Physics, Chinese Academy of Sciences (CAS), Beijing* 100190, *China*
[2] *University of Chinese Academy of Sciences, Beijing* 100490, *China*
[3] *School of Physics and Beijing Key Laboratory of Optoelectronic Functional Materials & MicroNano Devices, Renmin University of China, Beijing* 100872, *China*
[4] *Key Laboratory of Quantum State Construction and Manipulation (Ministry of Education), Renmin University of China, Beijing* 100872, *China*

(Received 3 April 2025; revised manuscript received 17 April 2025; accepted manuscript online 21 April 2025)

Intrinsic magnetic topological insulators have been reported to exhibit novel physical phenomena such as the quantum anomalous Hall effect and axion insulator states, demonstrating potential for applications in spintronics and topological quantum computing. Here we perform low-temperature scanning tunneling microscopy (STM) investigations of the antiferromagnetic ground state of $MnSb_2Te_4$, a predicted magnetic topological insulator isostructural with $MnBi_2Te_4$. We visualize the hexagonal Te-terminated surface of $MnSb_2Te_4$ and identify two distinct defects originating from different antisite substitutions. Notably, we identify an in-gap state above the Fermi energy where the tunneling spectrum exhibits a negative differential conductance behavior. This electronic state can be modulated by external electric and magnetic fields, suggesting effective pathways for electronic state manipulation. Spin-resolved STM measurements further reveal additional magnetic resonance peaks associated with Mn antisite defects. Our results provide novel insights into the investigation of magnetic topological insulators and demonstrate a promising approach to modulate the localized electronic states.

Keywords: magnetic topological insulator, antisite defects, tunable electronic states, scanning tunneling microscopy

PACS: 68.37.Ef, 75.50.Ee, 73.21.Ac, 07.79.Cz

DOI: 10.1088/1674-1056/adcea3 **CSTR:** 32038.14.CPB.adcea3

1. Introduction

Topological insulators are of great interest in condensed matter physics due to their unusual electronic properties and promising potential for low-power electronic devices.[1] When magnetic elements (such as a ferromagnetic layer) are introduced into a topological insulator, the interplay between magnetism and topological state will create a variety of intriguing quantum phenomena, such as the quantum anomalous Hall (QAH) effect with quantized Hall plateaus and dissipationless electron transport of edge states. The QAH effect was first observed in chromium-doped $(Bi,Sb)_2Te_3$ films at 30 mK.[2] In order to increase the critical temperature, many magnetic topological insulators (MTIs) are constructed subsequently.[3–7] One of the most studied MTIs is $MnBi_2Te_4$ ($MnBi_{2n}Te_{3n+1}$, $n = 1$), which can be simply regarded as superlattices between ferromagnetic insulator layers of MnTe and topological insulator layers of Bi_2Te_3.[8–10] The ground state of bulk $MnBi_2Te_4$ is an antiferromagnetic (AFM) topological insulator, exhibiting intralayer ferromagnetism and interlayer antiferromagnetism at low temperature. Gapless topological surface states (TSSs) are predicted to appear only at surfaces parallel to the magnetic moment.[11–16] However, recent angle-resolved photoemission spectroscopy measurements probe gapless TSSs at the top surface, suggesting magnetic reconstruction and TSSs redistribution.[17–23] For the AFM state of $MnBi_2Te_4$ thin films, even-number and odd-number septuple layers (SLs) of samples have completely different topological properties.[12,24] For the even-layered case, the magnetization vectors on the top and bottom surfaces are aligned parallel, resulting in an axion insulator with a topological magnetoelectric effect. [12,25–31] For the odd one, the direction of magnetization vectors is antiparallel, leading to a QAH insulator with gapless chiral edge channel.[12,29,32,33] Furthermore, the magnetic field can lead to a change in magnetic configuration from AFM to FM. The FM state of bulk $MnBi_2Te_4$ enters the magnetic Weyl semimetal state, while FM thin films exhibit QAH insulator behavior.[12,25]

Similar to $MnBi_2Te_4$, isostructural $MnSb_2Te_4$ is also

†Corresponding author. E-mail: hlei@ruc.edu.cn
‡Corresponding author. E-mail: zhongxuwei@iphy.ac.cn
§Corresponding author. E-mail: tqian@iphy.ac.cn

© 2025 Chinese Physical Society and IOP Publishing Ltd. All rights, including for text and data mining, AI training, and similar technologies, are reserved.

considered as a potential MTI. With mixing of Mn and Sb at different sites, the magnetic ground state of $MnSb_2Te_4$ can be tuned during crystal growth between AFM and FM states.[34–40] More antisite substitution defects can even induce spin glass behavior.[38] For the AFM state of bulk $MnSb_2Te_4$, magnetic susceptibility measurement shows a Néel temperature of 20 K.[36] Density functional theory calculations[41,42] indicate that the AFM order with trivial topological property of $MnSb_2Te_4$ is the lowest energy case. No topological states of $MnSb_2Te_4$ are detected by time- and angle-resolved photoemission spectroscopy measurements.[39] However, other members of the $MnSb_{2n}Te_{3n+1}$ family are considered as candidates for QAH insulators, axion insulators and Weyl semimetals.[43,44] For flakes of $MnSb_2Te_4$, polar reflectance magnetic circular dichroism spectroscopy experiments have observed the additional surface spin-flipping transitions in even-SL AFM samples, while abrupt bulk spin-flipping transitions are observed in FM samples.[45] As for the topological properties, observation of TSSs is reported in the Mn-rich FM state of bulk $MnSb_2Te_4$.[37] Axion insulating states are discovered in the bulk $MnSb_4Te_7$ and $MnSb_8Te_{13}$ by angle-resolved photoemission spectroscopy measurement.[46,47] It seems that AFM $MnSb_2Te_4$ is the ground state of these novel states, which motivates us to investigate its electronic structure.

In this work, we employ scanning tunneling microscopy / spectroscopy (STM/STS) to study the surface topography and electronic structure of single crystal $MnSb_2Te_4$. The exposed Te layer exhibits a hexagonal lattice with two types of antisite substitution defects. The tunneling spectrum exhibits a full gap of 480 meV, indicating the insulating characteristics. Zooming in on the gap region reveals that there is an in-gap $\mathrm{d}I/\mathrm{d}V$ peak located around 200 meV. Notably, surface defects exhibit a significantly enhanced $\mathrm{d}I/\mathrm{d}V$ peak compared to defect-free regions, accompanied by a negative differential conductance (NDC) feature. Further measurements reveal that the intensity and position of the peak corresponding to this in-gap state can be tuned by the tip-sample distance and magnetic field. In addition, we carry out spin-resolved STM experiments and find a new conductance peak and a NDC region at higher energy, which can also be modulated by magnetic field and needs further study. Our work carefully investigates the electronic structure of $MnSb_2Te_4$ and provides a basis for a comprehensive understanding of the $MnSb_{2n}Te_{3n+1}$ family.

2. Material and methods

High-quality single crystal of antiferromagnetic $MnSb_2Te_4$ was prepared using the self-flux method.[45] STM/S experiments were performed in an ultrahigh low temperature USM-1300-^{3}He system (Unisoku Co., Ltd., Japan) with a 16 T magnet in the Synergetic Extreme Condition User Facility, Beijing, China. The $MnSb_2Te_4$ samples were cleaved in an ultrahigh vacuum ($\sim 6.0\times10^{-10}$ Torr) at room temperature, and then transferred to the scanner head kept at around 4.3 K. All STM/S experiments were carried out at 4.3 K. Pt/Ir tips and Cr tips were used after electron-beam heating and calibration on the Ag (100) surface. Topographic images were obtained by the constant-current mode. The tunneling spectra were measured using a standard lock-in technique at a frequency of 973.7 Hz. The direction of the applied magnetic field was parallel to the c-axis of the sample.

3. Results and discussion

The layered material $MnSb_2Te_4$ is isostructural to $MnBi_2Te_4$, obeying the symmetries of R-3m space group (No. 166). As illustrated in Fig. 1(a), the intercalation of MnTe layers into Sb_2Te_3 forms septuple layers that are stacked along the c-axis and bound by van der Waals interactions. Under ultrahigh vacuum conditions, the sample is cleaved between two adjacent septuple layers, generating atomically flat Te-terminated surfaces, as shown in Fig. 1(a). In the top view, adjacent Te monolayers form a honeycomb lattice. The Mn atomic magnetic moments within each septuple layer align ferromagnetically, while neighboring septuple layers exhibit antiferromagnetic interlayer coupling with opposing magnetic orientations. Figure 1(b) presents the STM topography image of the cleaved $MnSb_2Te_4$ surface, revealing the hexagonal lattice of Te atoms. The fast Fourier transform analysis (inset of Fig. 1(b)) confirms sixfold-symmetric Bragg wavevectors with the lattice constant measured as 0.43 nm, consistent with prior x-ray diffraction experimental reports.[45] Figure 1(c) shows a zoom-in atomically resolved image distinguishing two distinct defect types. Based on previous studies of $MnBi_2Te_4$,[48] the bright dots in the right inset are attributed to antisite defects where surface Te atoms are substituted by Mn or Sb atoms, while the dark triangles in the left inset originate from Mn substitutions at Sb sites in the second atomic layer beneath the cleaved surface. Moreover, regarding the six surrounding triangles of the surface Te hexagonal lattice, three of the triangle centers correspond to Sb in the second layer below. As illustrated in Fig. 1(c), all of the dark triangles exhibit a consistent orientation, indicating the atomic origin of the defects from Sb sites. Both types of defects are distributed irregularly across the surface, showing a high defect density of 38%.

Scanning tunneling spectroscopy can directly reflect the local electronic density of states by measuring the $\mathrm{d}I/\mathrm{d}V$. Figure 2(a) illustrates a typical tunneling spectrum of $MnSb_2Te_4$, where the highest occupied state is located at

−120 meV, while the unoccupied state is detected at 360 meV above the Fermi energy level. The energy gap size is determined to be 480 meV. The inset of Fig. 2(a) shows more details that a dI/dV peak is detected at 200 meV in the gap. Note that when the tip approaches sufficiently close to the surface, the localized tip-induced electric field can modulate the sample's density of states. We collect tunneling spectra under different bias voltages (V_B) and summarize them in Fig. 2(b). Using the same setpoint of tunneling current (I_t = 300 pA), each starting voltage corresponds to a distinct tip height due to the feedback-controlled mechanism of STM. The collected three curves overlap within the error, demonstrating that the tip effect is negligible and the intrinsic properties of electronic structure are detected.

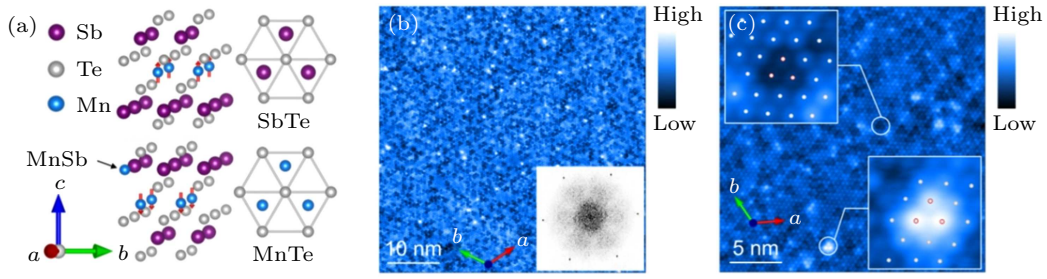


Fig. 1. Lattice structure and surface characterization of $MnSb_2Te_4$. (a) Side view and top view of crystal structure of $MnSb_2Te_4$. A Mn_{Sb} antisite defect is marked illustratively. (b) Large-scale STM topographic image of $MnSb_2Te_4$, showing the atomic structures of the Te surface (size 50×50 nm, bias voltage $V_B = -0.6$ V, tunneling current $I_t = 500$ pA). Insert: The magnitude of Fourier transforms, exhibiting six-fold symmetry. (c) Atomically resolved STM topographic image of $MnSb_2Te_4$ (size 25×25 nm, $V_B = -0.55$ V, $I_t = 300$ pA). Insert: Two types of antisite defects, which can be identified as dark triangles and bright dots.

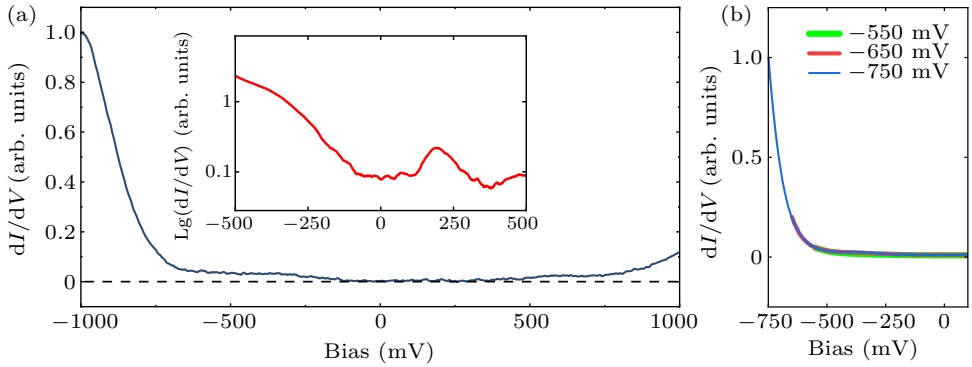


Fig. 2. Electronic localized density of state spectra of $MnSb_2Te_4$. (a) The tunneling spectra taken at the Te surface, showing high density of electronic state at bias voltage $V_B < -120$ mV and $V_B > 360$ mV. Data inset exhibits a peak at $V_B = 200$ mV in the gap. (b) The tunneling spectra taken from different bias voltages. The bias voltages of the blue, red and green curves are −750 mV, −650 mV and −550 mV, respectively. The setpoint of tunneling current is 300 pA. The curves are set to different thicknesses for clear comparison.

To further investigate the effect of defects on electronic structure, we performed spatially resolved tunneling spectroscopy at several typical regions. Figure 3(b) presents tunneling spectra acquired at six points marked in the atomically resolved topography as shown in Fig. 3(a). Similar to other MTIs, the AFM ground state of $MnSb_2Te_4$ exhibits pronounced spatial variations in the localized density of states. The bright antisite defects and partially defect-free areas display a prominent differential conductance peak at 200 mV, accompanied by a NDC region. In contrast, the conductance peak becomes significantly suppressed at dark triangular antisite defects. The emergence of NDC signifies an anomalous region where increasing the bias voltage leads to a decrease in tunneling current, as shown in Fig. 3(c). Similar phenomena have been observed in isolated atoms,[49,50] molecular electronic devices,[51–53] and surface states of two-dimensional materials,[54] where the usual origin is the resonant tunneling structure through a narrow band like an atomic energy level. In contrast, the dI/dV peak becomes significantly suppressed at dark triangular antisite defects. Figure 3(d) schematically illustrates the tunneling process through in-gap states under varying bias voltages. Adjusting the bias voltage alters the relative chemical potential between the tip and sample, corresponding to distinct tunneling energy regions. When the tip's chemical potential aligns with the sample's valence band, tunneling occurs with conductance intensity reflecting the localized density of states. During the bias voltage increase, positioning the tip's chemical potential within the sample's gap suppresses the tunneling current (green region in Fig. 3(d)). Subsequent alignment with the in-gap state induces abrupt dI/dV rise by narrow-band resonant tunneling (red region in Fig. 3(d)). When the tip's chemical potential traverses the maximum density of states, the tunneling current decreases, generating the NDC region (blue region in Fig. 3(d)).

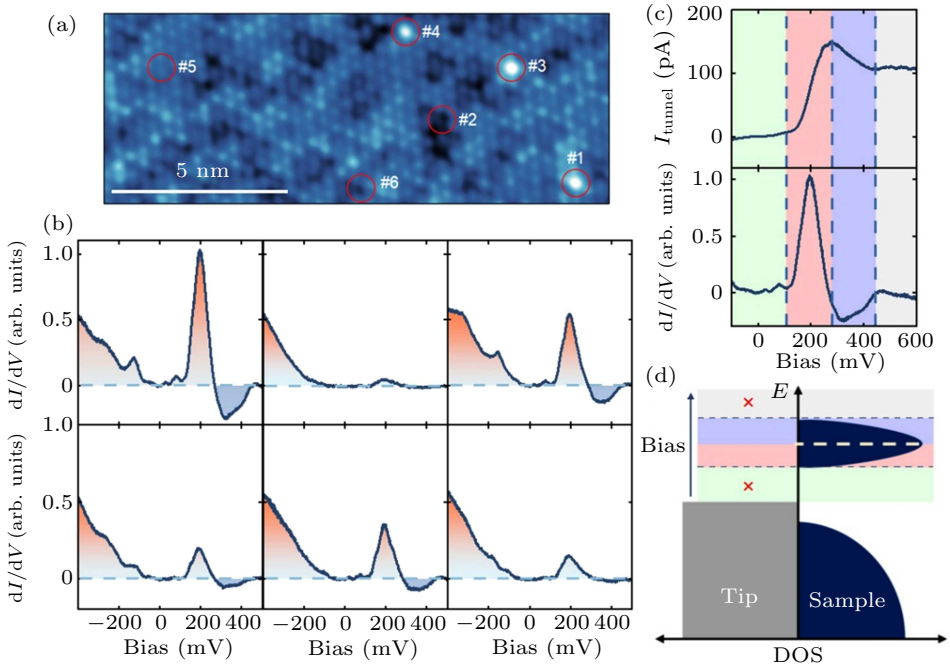


Fig. 3. Spatial fluctuating features of tunneling spectra and NDC regions. (a) Atomically resolved STM topographic image of Te-terminated surface (size 15×5.5 nm, bias voltage $V_B = -0.6$ V, tunneling current $I_t = 400$ pA). (b) Typical tunneling spectra taken at the locations marked by the red circles in (a). NDC regions are marked with blue shadow. (c) Measured I_t vs. V_B curve and tunneling spectra taken on the bright defect in (a), showing a strong tunneling spectra peak that centers at bias voltage $V_B = 0.2$ V (red region). A region of NDC follows the peak at higher bias, showing anomalous tunneling current behavior (blue region). (d) Schematic illustration of $\mathrm{d}I/\mathrm{d}V$ vs. energy. Increasing the bias raises the chemical potential of the tip, corresponding to the different regions in (c). The red cross indicates the energy region where the DOS of $MnSb_2Te_4$ is negligible. The red region represents the tunneling current when the in-gap state is partially filled. The blue region represents the anomaly tunneling current corresponding to NDC phenomenon.

To investigate the nature of the localized in-gap states, we further modulated the electronic states using electric and magnetic fields. Figure 4(a) presents consecutive tunneling spectra acquired at the same location under identical conditions (bias $V_B = -600$ mV, tunneling current $I_t = 400$ pA). The emergence of two distinct spectral configurations demonstrates that the tip-induced electric field modulates the localized electronic states. Repeated tunneling spectral collections under identical conditions reveal reversible switching between these two configurations, indicating the in-gap states' transitions. Comparative analysis of the two spectra reveals a ~ 30 meV shift in valence band features and a ~ 50 meV shift of the in-gap state, suggesting the changes in both the localized chemical potential and the in-gap state of the sample. Figure 4(b) illustrates the evolution of in-gap state at dark triangular antisite defects under vertical magnetic fields. The $\mathrm{d}I/\mathrm{d}V$ peak intensity increases and its position moves 35 mV toward the valence band, while this shift slightly amplifies with increasing magnetic field. Furthermore, the negative conductance becomes enhanced, likely arising from magnetic field-induced narrowing of the in-gap state bandwidth, resulting in more drastic changes in tunneling current.

The shift of the resonance peak under the magnetic field indicates the magnetic nature of the in-gap state. We then carry out spin-resolved STM measurements by a Cr tip. Figure 4(c) displays the atomically resolved STM topography obtained with the Cr tip. Tunneling spectra reveal a strong differential conductance peak at 330 mV accompanied by a NDC region, along with a kink at 200 mV corresponding to the in-gap state peak observed with Pt/Ir tips (Fig. 4(d)). Remarkably, the peak position remains invariant under varying tunneling currents (i.e., tip–sample distances). The spin selectivity of the Cr tip, which permits tunneling only for electrons with spin parallel to the tip's magnetization, substantially suppresses the conductance peak intensity of the in-gap state. Figure 4(e) presents $\mathrm{d}I/\mathrm{d}V$ mapping at the energy of the conductance peak, demonstrating that the conductance peak mainly emerges at dark triangular antisite defects (black box in Fig. 4(e) and white box in Fig. 4(c)). This spatial correlation suggests an origin linked to second-layer Mn atomic magnetic moments. A plausible explanation is the Ruderman–Kittel–Kasuya–Yosida (RKKY) interaction, where exchange coupling between subsurface Mn moments and surface electrons induces spin splitting of electronic states, creating spin-polarized resonance peaks detectable by the spin-selective tip. Figure 4(f) reveals a 30 meV energy separation between conductance peaks associated with opposite spin channels. The RKKY effect introduces an effective exchange field at the Mn antisite defects through the spin polarization of the conduction electrons, leading to a splitting of the spin energy levels in the localized state. Spin-resolved measurements capture the splitting of the energy levels corresponding to the different spin orientations, which is manifested as a difference in the resonance peak positions. Differences in tunneling spectra obtained by Cr tips and Pt–Ir tips need further investigation.

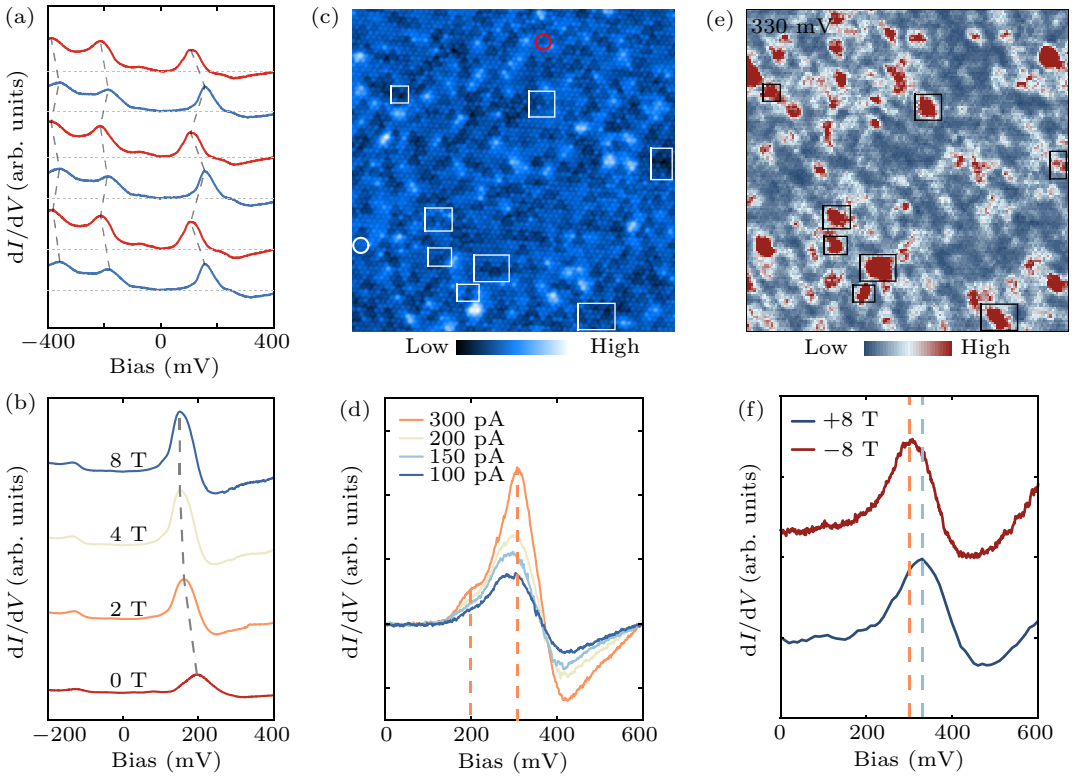


Fig. 4. Response of tunneling spectra in electric field and magnetic field. (a) Tip-induced electric field leads to a shift of the chemical potential and modulations of electronic states. Each curve is shifted vertically for clarity. (b) External magnetic field leads to a movement of resonance peak. Each curve is shifted vertically for clarity. (c) Atomically resolved STM topographic image (size 25×25 nm, bias voltage $V_B = -0.55$ V, tunneling current $I_t = 300$ pA) obtained using a Cr-tip. (d) Spin-resolved tunneling spectra taken at the location marked by the red circle in (c), showing a strong peak that centers at $V_B = 0.3$ V and a kink at $V_B = 0.2$ V. A region of NDC follows the strong peak at higher V_B. (e) $\mathrm{d}I/\mathrm{d}V$ mapping taken at $V_B = 0.33$ V, showing the spatial distribution of differential conductance peaks. The black boxes demonstrate regions exhibiting significant $\mathrm{d}I/\mathrm{d}V$ enhancements, consistent with the regions marked by white boxes in (c). (f) Tunneling spectra measured by the Cr tip with opposite spin direction taken at the location marked by the white circle in (c), displaying a 30 meV difference between the two peaks.

4. Conclusion and perspectives

In conclusion, we systematically investigate the interplay among antisite defects, localized in-gap states, and magnetic interactions in $MnSb_2Te_4$. Our findings demonstrate that while the AFM ground state of $MnSb_2Te_4$ is topologically trivial, a distinct in-gap state appears above the valence band. Atomic-scale tunneling spectroscopy reveals that the in-gap state manifests as a differential conductance peak accompanied by NDC. The origin of the localized in-gap states warrants further theoretical investigation. Notably, tip-induced electric fields modulate the energy of in-gap states. Under the vertical magnetic field, the in-gap states at dark triangular antisite defects exhibit bandwidth narrowing and enhanced NDC. Spin-resolved experiments using a Cr tip reveal spin-selective tunneling resonances distinct from conventional tip measurements, linking these features to the magnetic origin of dark defects. The observation confirms that dark defects correspond to Mn substitutions at Sb sites. Our work provides a novel method for studying antisite defects in $MnSb_2Te_4$. This approach can be extended to explore other $MnSb_2Te_4$-family compounds, elucidating the intricate relationships among topological structure, surface characteristics, and magnetic interactions. Additionally, the ability to modulate in-gap states via external fields suggests potential applications in spintronic devices and quantum information technologies, paving the way for future research in defect-engineered magnetic topological insulators.

Acknowledgements

Project supported by the National Key R&D Program of China (Grant Nos. 2022YFA1403800 and 2023YFA1406500) and the National Natural Science Foundation of China (Grant No. 12274459).

References

[1] Tokura Y, Yasuda K and Tsukazaki A 2019 *Nat. Rev. Phys.* **1** 126
[2] Chang C Z, Zhang J, Feng X, Shen J, Zhang Z, Guo M, Li K, Ou Y, Wei P, Wang L L, Ji Z Q, Feng Y, Ji S, Chen X, Jia J, Dai X, Fang Z, Zhang S C, He K, Wang Y, Lu L, Ma X C and Xue Q K 2013 *Science* **340** 167
[3] Checkelsky J G, Yoshimi R, Tsukazaki A, Takahashi K S, Kozuka Y, Falson J, Kawasaki M and Tokura Y 2014 *Nat. Phys.* **10** 731
[4] Chang C Z, Zhao W, Kim D Y, Zhang H, Assaf B A, Heiman D, Zhang S C, Liu C, Chan M H W and Moodera J S 2015 *Nat. Mater.* **14** 473
[5] Mogi M, Yoshimi R, Tsukazaki A, Yasuda K, Kozuka Y, Takahashi K S, Kawasaki M and Tokura Y 2015 *Appl. Phys. Lett.* **107** 182401
[6] Ou Y, Liu C, Jiang G, Feng Y, Zhao D, Wu W, Wang X X, Li W, Song C, Wang L L, Wang W, Wu W, Wang Y, He K, Ma X C and Xue Q K 2018 *Adv. Mater.* **30** 1703062
[7] Wang Q, Zhao J, Wu W, Zhou Y, Li Q, Edmonds M T and Yang S A 2023 *Chin. Phys. B* **32** 087506
[8] Burkov A A and Balents L 2011 *Phys. Rev. Lett.* **107** 127205

[9] He K 2020 *Npj Quantum Mater.* **5** 1

[10] Dong X, Jia X, Yan Z, Shen X, Li Z, Qiao Z and Xu X 2023 *Chin. Phys. Lett.* **40** 087301

[11] Mong R S K, Essin A M and Moore J E 2010 *Phys. Rev. B* **81** 245209

[12] Zhang D, Shi M, Zhu T, Xing D, Zhang H and Wang J 2019 *Phys. Rev. Lett.* **122** 206401

[13] Gong Y, Guo J, Li J, Zhu K, Liao M, Liu X, Zhang Q, Gu L, Tang L, Feng X, Zhang D, Li W, Song C, Wang L, Yu P, Chen X, Wang Y, Yao H, Duan W, Xu Y, Zhang S C, Ma X, Xue Q K and He K 2019 *Chin. Phys. Lett.* **36** 076801

[14] Otrokov M M, Klimovskikh I I, Bentmann H, Estyunin D, Zeugner A, Aliev Z S, Gaß S, Wolter A U B, Koroleva A V, Shikin A M, Blanco-Rey M, Hoffmann M, Rusinov I P, Vyazovskaya A Y, Eremeev S V, Koroteev Y M, Kuznetsov V M, Freyse F, Sánchez-Barriga J, Amiraslanov I R, Babanly M B, Mamedov N T, Abdullayev N A, Zverev V N, Alfonsov A, Kataev V, Büchner B, Schwier E F, Kumar S, Kimura A, Petaccia L, Di Santo G, Vidal R C, Schatz S, Kißner K, Ünzelmann M, Min C H, Moser S, Peixoto T R F, Reinert F, Ernst A, Echenique P M, Isaeva A and Chulkov E V 2019 *Nature* **576** 416

[15] Vidal R C, Bentmann H, Peixoto T R F, Zeugner A, Moser S, Min C-H, Schatz S, Kißner K, Ünzelmann M, Fornari C I, Vasili H B, Valvidares M, Sakamoto K, Mondal D, Fujii J, Vobornik I, Jung S, Cacho C, Kim T K, Koch R J, Jozwiak C, Bostwick A, Denlinger J D, Rotenberg E, Buck J, Hoesch M, Diekmann F, Rohlf S, Kalläne M, Rossnagel K, Otrokov M M, Chulkov E V, Ruck M, Isaeva A and Reinert F 2019 *Phys. Rev. B* **100** 121104

[16] Lee S H, Zhu Y, Wang Y, Miao L, Pillsbury T, Yi H, Kempinger S, Hu J, Heikes C A, Quarterman P, Ratcliff W, Borchers J A, Zhang H, Ke X, Graf D, Alem N, Chang C Z, Samarth N and Mao Z 2019 *Phys. Rev. Res.* **1** 012011

[17] Chen Y J, Xu L X, Li J H, Li Y W, Wang H Y, Zhang C F, Li H, Wu Y, Liang A J, Chen C, Jung S W, Cacho C, Mao Y H, Liu S, Wang M X, Guo Y F, Xu Y, Liu Z K, Yang L X and Chen Y L 2019 *Phys. Rev. X* **9** 041040

[18] Hao Y J, Liu P, Feng Y, Ma X M, Schwier E F, Arita M, Kumar S, Hu C, Lu R, Zeng M, Wang Y, Hao Z, Sun H Y, Zhang K, Mei J, Ni N, Wu L, Shimada K, Chen C, Liu Q and Liu C 2019 *Phys. Rev. X* **9** 041038

[19] Li H, Gao S Y, Duan S F, Xu Y F, Zhu K J, Tian S J, Gao J C, Fan W H, Rao Z C, Huang J R, Li J J, Yan D Y, Liu Z T, Liu W L, Huang Y B, Li Y L, Liu Y, Zhang G B, Zhang P, Kondo T, Shin S, Lei H C, Shi Y G, Zhang W T, Weng H M, Qian T and Ding H 2019 *Phys. Rev. X* **9** 041039

[20] Nevola D, Li H X, Yan J Q, Moore R G, Lee H N, Miao H and Johnson P D 2020 *Phys. Rev. Lett.* **125** 117205

[21] Swatek P, Wu Y, Wang L L, Lee K, Schrunk B, Yan J and Kaminski A 2020 *Phys. Rev. B* **101** 161109

[22] Yan C, Fernandez-Mulligan S, Mei R, Lee S H, Protic N, Fukumori R, Yan B, Liu C, Mao Z and Yang S 2021 *Phys. Rev. B* **104** L041102

[23] Wang Y, Ma X M, Hao Z, Cai Y, Rong H, Zhang F, Chen W, Zhang C, Lin J, Zhao Y, Liu C, Liu Q and Chen C 2024 *Natl. Sci. Rev.* **11** nwad066

[24] Yang S, Xu X, Zhu Y, Niu R, Xu C, Peng Y, Cheng X, Jia X, Huang Y, Xu X, Lu J and Ye Y 2021 *Phys. Rev. X* **11** 011003

[25] Li J, Li Y, Du S, Wang Z, Gu B L, Zhang S C, He K, Duan W and Xu Y 2019 *Sci. Adv.* **5** eaaw5685

[26] Otrokov M M, Rusinov I P, Blanco-Rey M, Hoffmann M, Vyazovskaya A Yu, Eremeev S V, Ernst A, Echenique P M, Arnau A and Chulkov E V 2019 *Films Phys. Rev. Lett.* **122** 107202

[27] Ge J, Liu Y, Li J, Li H, Luo T, Wu Y, Xu Y and Wang J 2020 *Natl. Sci. Rev.* **7** 1280

[28] Deng Y, Yu Y, Shi M Z, Guo Z, Xu Z, Wang J, Chen X H and Zhang Y 2020 *Science* **367** 895

[29] Gao A, Liu Y F, Hu C, Qiu J X, Tzschaschel C, Ghosh B, Ho S C, Bérubé D, Chen R, Sun H, Zhang Z, Zhang X Y, Wang Y X, Wang N, Huang Z, Felser C, Agarwal A, Ding T, Tien H J, Akey A, Gardener J, Singh B, Watanabe K, Taniguchi T, Burch K S, Bell D C, Zhou B B, Gao W, Lu H Z, Bansil A, Lin H, Chang T R, Fu L, Ma Q, Ni N and Xu S Y 2021 *Nature* **595** 521

[30] Lin W, Feng Y, Wang Y, Zhu J, Lian Z, Zhang H, Li H, Wu Y, Liu C, Wang Y, Zhang J, Wang Y, Chen C Z, Zhou X and Shen J 2022 *Nat. Commun.* **13** 7714

[31] Li Y, Wang Y, Lian Z, Li H, Gao Z, Xu L, Wang H, Lu R, Li L, Feng Y, Zhu J, Liu L, Wang Y, Fu B, Yang S, Yang L, Wang Y, Xia T, Liu C, Jia S, Wu Y, Zhang J, Wang Y and Liu C 2024 *Nat. Commun.* **15** 3399

[32] Qi X L, Hughes T L and Zhang S C 2008 *Phys. Rev. B* **78** 195424

[33] He Q L, Hughes T L, Armitage N P, Tokura Y and Wang K L 2022 *Nat. Mater.* **21** 15

[34] Xi M and Lei H 2024 *Chin. Phys. B* **33** 067503

[35] Murakami T, Nambu Y, Koretsune T, Xiangyu G, Yamamoto T, Brown C M and Kageyama H 2019 *Phys. Rev. B* **100** 195103

[36] Liu Y, Wang L L, Zheng Q, Huang Z, Wang X, Chi M, Wu Y, Chakoumakos B C, McGuire M A, Sales B C, Wu W and Yan J 2021 *Phys. Rev. X* **11** 021033

[37] Wimmer S, Sánchez-Barriga J, Küppers P, Ney A, Schierle E, Freyse F, Caha O, Michalička J, Liebmann M, Primetzhofer D, Hoffman M, Ernst A, Otrokov M M, Bihlmayer G, Weschke E, Lake B, Chulkov E V, Morgenstern M, Bauer G, Springholz G and Rader O 2021 *Adv. Mater.* **33** 2102935

[38] Ge W, Sass P M, Yan J, Lee S H, Mao Z and Wu W 2021 *Phys. Rev. B* **103** 134403

[39] Xi M, Chen F, Gong C, Tian S, Yin Q, Qian T and Lei H 2022 *J. Phys. Chem. Lett.* **13** 10897

[40] Xiong J, Peng Y H, Lin J Y, Cen Y J, Yang X B and Zhao Y J 2023 *Materials* **16** 5496

[41] Chen L, Wang D, Shi C, Jiang C, Liu H, Cui G, Zhang X and Li X 2020 *J. Mater. Sci.* **55** 14292

[42] Zhou L, Tan Z, Yan D, Fang Z, Shi Y and Weng H 2020 *Phys. Rev. B* **102** 085114

[43] Huan S, Wang D, Su H, Wang H, Wang X, Yu N, Zou Z, Zhang H and Guo Y 2021 *Appl. Phys. Lett.* **118** 192105

[44] Eremeev S V, Rusinov I P, Koroteev Yu M, Vyazovskaya A Yu, Hoffmann M, Echenique P M, Ernst A, Otrokov M M and Chulkov E V 2021 *J. Phys. Chem. Lett.* **12** 4268

[45] Zang Z, Zhu Y, Xi M, Tian S, Wang T, Gu P, Peng Y, Yang S, Xu X, Li Y, Han B, Liu L, Wang Y, Gao P, Yang J, Lei H, Huang Y and Ye Y 2022 *Phys. Rev. Lett.* **128** 017201

[46] Huan S, Zhang S, Jiang Z, Su H, Wang H, Zhang X, Yang Y, Liu Z, Wang X, Yu N, Zou Z, Shen D, Liu J and Guo Y 2021 *Phys. Rev. Lett.* **126** 246601

[47] Mudgal M, Dutta D, Meena P, Yenugonda V, Tiwari V K, Malik V K, Buck J, Mahatha S K, Agarwal A and Nayak J 2024 *Phys. Rev. B* **110** 045124

[48] Yuan Y, Wang X, Li H, Li J, Ji Y, Hao Z, Wu Y, He K, Wang Y, Xu Y, Duan W, Li W and Xue Q K 2020 *Nano Lett.* **20** 3271

[49] Lyo I W and Avouris P 1989 *Science* **245** 1369

[50] Xue Y, Datta S, Hong S, Reifenberger R, Henderson J I and Kubiak C P 1999 *Phys. Rev. B* **59** R7852

[51] Britnell L, Gorbachev R V, Geim A K, Ponomarenko L A, Mishchenko A, Greenaway M T, Fromhold T M, Novoselov K S and Eaves L 2013 *Nat. Commun.* **4** 1794

[52] Kim K S, Kim T H, Walter A L, Seyller T, Yeom H W, Rotenberg E and Bostwick A 2013 *Phys. Rev. Lett.* **110** 036804

[53] Xu B and Dubi Y 2015 *J. Phys. Condens. Matter* **27** 263202

[54] Liu X R, Deng H, Liu Y, Yin Z, Chen C, Zhu Y P, Yang Y, Jiang Z, Liu Z, Ye M, Shen D, Yin J X, Wang K, Liu Q, Zhao Y and Liu C 2023 *Nat. Commun.* **14** 2905